Rupture phase in near-fault records of the 2023 Turkey Mw 7.8 earthquake

Suli Yao (suliyao@cuhk.edu.hk) and Hongfeng Yang*(hyang@cuhk.edu.hk)

Earth and Environmental Sciences Programme, Chinese University of Hong Kong, Hong Kong, China

This is a non-peer reviewed preprint submitted to EarthArXiv

Abstract:

Understanding and deciphering wiggles especially coherent phases from seismograms have been a long endeavor to understand the earth structure and earthquake source. However, coherent phases directly associated with earthquake rupture propagation have not been available due to the lack of continuous near-fault observations. Here we report the rupture phase as large velocity pulses during the 2023 Mw 7.8 Turkey earthquake. Through data analysis and numerical rupture simulations, we estimate the rupture speed to be subshear (i.e. ~3.1-3.4 km/s) along the southern segment of the East Anatolian Fault. Moreover, we constrain the critical slip distance (D_c) to be ~ 1.35 m in average, 60% of the reported average surface slip. With the expanding coverage of near-fault observation network, such rupture phases in future earthquakes can be used to unravel rupture process and frictional properties on faults.

One Sentence Summary:

The near-fault rupture phases as velocity pulses in the 2023 Mw 7.8 Turkey earthquake reveal earthquake rupture propagation.

Main Text:

Seismic waves are generated by activities with sudden movements inside or on the surface of the earth such as earthquakes, volcanos, and landslides. The waves propagate inside the earth and therefore carry the info of both the source and the earth structure. It has been long known to discover the Earth internal structure by directly tracking coherent wave phases on seismograms and projecting them to velocity discontinuities at certain depths, as demonstrated by numerous textbook examples such as the discovery of the Moho *(1)* and the solid inner core *(2)*. In addition to structure imaging, the seismic wave phases can also offer direct information about earthquake source, such as the location and the radiation pattern that indicates source mechanisms.

Compared to earthquake location and focal mechanism, resolving earthquake rupture process is more challenging. The seismic waves received on the ground surface are the superposition of response to continuous rupture process, convolving with earth structure. Efforts have been made to understand rupture propagation from seismic waves, mostly based on finite-fault slip inversion *(3,4)* and back-projection *(5)* approaches. The former utilizes Green's functions to link the slip on the fault to surface responses. Certain assumptions on the source process are needed, such as the path of the rupture front and the shape of the slip rate function, which potentially lead to intrinsic uncertainties *(6,7)*. Back-projection only demands waveform stacking to locate where the energy was radiated. However, whether the radiated energy robustly represents the rupture front is ambiguous and the results sometimes depend on array geometry and frequency content *(8,9)*. Similar approache can be applied to near-field arrays. For instance, Spudich and Cranswick (1984) applied sliding-window cross correlation to track the rupture propagation of the 1979 Mw 6.9 Imperial Valley earthquake, using data on a 213-m-long array of 5 strong motion stations that were located 5.6 km from the fault trace *(10)*.

Stations located very close to faults are anticipated to reveal the rupture propagation directly (Fig.1). During rupture propagation, points on the fault start to slip when the rupture front reaches and rises the shear stress to the yield stress (τ_s). Then the slip shall accelerate with the reduction of frictional resistance, known as coseismic weakening *(11)*, and reach a stable stage until the frictional resistance gets to the lowest level (dynamic stress, τ_d) (Fig.1a). Correspondingly, slip rate on the fault displays a pulse with the peak time associated with the weakening time *(12)* (Fig.1a). On the ground, if the distance from the station to the fault is sufficiently close, the near-fault stations should record a large velocity pulse when the rupture front passes. The pulse, termed the rupture phase, carries information of the local fault slip rate evolution and the weakening process *(13)*.

Although the rupture phases are commonly viewed in dynamic rupture simulations *(14,15)*, observations of rupture phases to date are mostly from laboratory experiments with sensor arrays on or near the frictional interfaces *(16)* or with ultrahigh-speed camera and digital imaging technique *(17)*. Direct observations of rupture phases in the field have been rare and most time are only available on one single station *(18-20)*, making it impossible to directly track the rupture. Here we for the first time report a coherent and robust observation of rupture phases during the 2023 Mw 7.8 Kahramanmaras earthquake in Turkey, from which we can derive rupture speed and in-situ frictional properties directly.

Observed rupture phase on near-fault strong motion stations

On 6 Feb 2023, at 01:17 UTC, an Mw 7.8 strike-slip earthquake initiated at 37.0234° E, 37.2444° N, at the depth of 12 km *(21)*, on a splay branch fault of the East-Anatolian fault (EAF), the transform boundary between the Anatolian and Arabian plates. The rupture then transitioned into the EAF and propagated bilaterally with a final along-strike extent of ~300 km. Around 9 hours later, an Mw 7.5 earthquake occurred on another fault ~100 km northwest of the mainshock epicenter. These two events, together with several M6 aftershocks, caused tremendous damage to buildings and facilities with violent ground shaking in Turkey and Syria. At the moment of writing, at least 55,700 deaths were reported, making it one of the deadliest natural hazards.

The 2023 Turkey sequence was well recorded by the local strong motion stations. For the mainshock, in total 50 stations with good records are available within 50 km from the fault trace (Fig. 2a). In particular, there are 10 stations located within 3 km to the ruptured surface trace of the southern segment (Fig. 2a), providing an unprecedented opportunity to investigate earthquake rupture process. We first rotate the waveforms from N-S and E-W components to fault-parallel (F-P) and fault-normal (F-N) components using the local strike for each station. The average strike among stations is ~26°. Then we obtain the velocity waveforms by integrating the acceleration. The peak amplitudes of the velocity waveforms range from 0.5 to 2.0 m/s (Fig. 2b and 2c). The timings of peaks in the two horizontal components are mostly consistent except on the three southernmost stations (3145, 3139, and 3142), where waveforms show more complex phases (Fig. 2b and 2c) that are likely due to impacts of the local fault geometry (Fig. 2a). Furthermore, we observe that velocity pulses in the F-N component are stronger than the F-P component, which is a typical characteristic of sub-shear ruptures *(22)*.

By aligning them according to the along-strike distances, the waveforms show a clear propagation of the velocity pulses with a speed of 3.1 km/s (Fig. 2b and 2c).

To investigate the potential causes of these velocity pulses, we first compare with the waveforms (Fig.S1) of an Mw 6.3 aftershock that occurred in the south (Fig. 2a). The travel times of P and S waves indicate a robust estimate on Vp of ~ 6.2 km/s and Vs of ~3.5 km/s, respectively, along the southern segment of the mainshock rupture (Fig.S1b). Moreover, the waves decay rapidly with distance in their amplitudes (Fig. S1a), while the velocity pulses observed during the mainshock don't, indicating that they were not S waves or multiples. Moreover, we calculate the spectrograms for the mainshock waveforms and find no dispersion during the large velocity pulses (Fig. S2 & S3). Thus, these pulses can not be surface waves either. As such, we propose that the velocity pulses are directly correlated with the rupture front propagation, i.e. rupture phases.

Dynamic rupture simulation for the Mw 7.8 Turkey earthquake

We conduct a 3-D dynamic rupture simulation to examine the correlation between the velocity pulses and the earthquake dynamic characteristics. Although our model is generic, we follow the geometry of the EAF ruptured during the Turkey earthquake, neglecting the branch where the earthquake was initiated *(21)*. We nucleate the rupture at the junction point between the branch and the main fault, nearly 30 km north to the bending point (Fig. S4a). The fault is set to be vertical, and the fault trace adopted in our model is determined by InSAR image (the thick black line in figure 2a). Frictional strength, initial stress, and dynamic stress are all set uniform. We assume a half-space velocity model with Vs of 3.5 km/s and Vp of 6.2 km/s. Other details of the model can be found in Supplementary Materials. Despite the simply generic model, the results capture the first-order features of the Mw 7.8 Turkey earthquake including the magnitude, rupture extent, and surface offset *(23)* (Fig. S4). The total duration of the rupture is ~50 s, consistent with the kinematic inversion results based on the regional high-rate GNSS and strong motion data *(21)* excluding the small amplitude pulse at the beginning which is associated with the initial stage of rupture on the branch.

In our model, the rupture propagates outside the nucleation zone with a circular rupture front. After getting saturated in depth, the rupture propagates along strike bilaterally (Fig. S4a). We then inspect the synthetic ground velocity waveforms at distance of 1 km from the fault trace and mark the peak time of velocity pulses (Fig. S5). The peaks of the velocities always occur very close to the true rupture front identified from slip rate evolution on fault (Fig. S5). The two differs in 1-2 seconds at different locations. The rupture speed on the fault is 3.19 km/s and 3.27 km/s on the northern and southern segments, respectively. In contrast, the rupture phase speed is 3.05 and 3.10 km/s, respectively (Fig. S5).

We also estimate the rupture phase speed at different distances to the fault and find that the estimates can be unstable when the distance is over 3 km (Fig. S6), due to the loss of coherence in waveform phases (Fig. S7). As the rupture is sub-shear, the radiated energy from the ruptured area will arrive before the rupture front and possibly contaminate the waveforms, moving the peaks slightly ahead and thus affecting the speed estimation. We further test models with different rupture speeds on faults (sub-shear or super-shear) and estimate the potential deviation of the rupture phase speeds (Table S1). The results indicate an underestimation within 7% (Fig. S8). Considering the rupture phase speed of 3.1 km/s shown in the data, the true average rupture speed of the Turkey earthquake is predicted to be 3.1-3.4 km/s along the southern segment, less than the S wave velocity inferred from the Mw 6.3 aftershock data. This inferred range is consistent with the rupture speed reported by the kinematic model constrained by local high-rate GNSS and strong motion data *(21)* (i.e., 3.2 km/s). As our data only cover the southern segment, we do not have constraints on the initial stage of the rupture on the branch fault, which was suggested to be in super-shear speed based on two near-fault strong motion stations *(24)*.

Discussion

Besides the rupture speed, the near-fault records can be used to constrain frictional properties on the fault. Following the method introduced in Fukuyama and Mikumo (2007) *(13)*, the critical slip distance, D_c, over which the frictional strength decreases from yield stress (τ_s) to dynamic stress (τ_d) , can be inferred directly as the double of ground displacement at the time of peak ground velocity in the F-P component, known as D_c''. Such approximation only works for records within a short distance to the fault as the sensitivity of ground velocity to the weakening process decays rapidly with distance *(25)*. This method has been applied to several earthquakes based on a single station within 3 km from the fault trace *(20)*. The 2023 Turkey earthquake makes it possible for the first time to obtain the D_c'' from 12 stations (an example in Fig. S9). However, the estimations of D_c'' on 5 stations are likely biased significantly by baseline shifts and the multiple peaks (see details in Supplementary materials). Here, we trust the stations with stable estimates and obtain the D_c'' to be 0.3-2.4 m (Fig. 3a). The average D_c'' is 1.35 m, ~60% of the average reported surface slip *(26)* (Fig. 3b and S10), nearly twice of the prediction from the empirical scaling law (Fig. 3b).

The near-fault strong motions can also help to resolve other frictional parameters, e.g. the strength drop ($\tau_s - \tau_d$). The strength drop is difficult to constrain mostly because of the trade-off with D_c in controlling the rupture process *(27)*. Now with the independent constraints on the D_c as discussed above, the strength drop can be solved through dynamic inversion *(28,29)* with constraints from the extensive near-field data. In our current model, we ignore the heterogeneous material properties inside the fault zone as we only try to capture the first order information of the rupture process. By considering fine velocity structure near the source region, future dynamic rupture models can be conducted to robustly constrain in-situ stress level and frictional properties of the fault ruptured during the 2023 Turkey earthquake. Furthermore, strong motion network has been rapidly expanding globally, making it possible to directly capture and investigate more rupture phases during future large earthquakes.

References

1. Mohorovičić, A., Das Beben Vom 8. x. 1909, *Jahrb. Meteorol. Observ. Zagreb*., 9, 1– 63 (1910).

2. Lehmann, I. "P'". Publications du Bureau Central Séismologique International. A14 (3): 87–115 (1936).

3. Das, S., & Kostrov, B. V. Inversion for seismic slip rate history and distribution with stabilizing constraints: Application to the 1986 Andreanof Islands earthquake. *Journal of Geophysical Research: Solid Earth,* 95(B5), 6899-6913 (1990).

4. Minson, S. E., Simons, M., & Beck, J. L Bayesian inversion for finite fault earthquake source models I—Theory and algorithm. *Geophysical Journal International,* 194(3), 1701-1726 (2013).

5. Ishii M., Shearer P.M., Houston H., Vidale J. E. Extent, duration and speed of the 2004 Sumatra–Andaman earthquake imaged by the Hi-net array. *Nature* 435:933–36 (2005).

6. Hartzell, S., Liu, P., Mendoza, C., Ji, C., & Larson, K. M.. Stability and uncertainty of finite-fault slip inversions: Application to the 2004 Parkfield, California, earthquake. *Bulletin of the Seismological Society of America*, *97*(6), 1911-1934 (2007).

7. Razafindrakoto, H. N., & Mai, P. M. Uncertainty in earthquake source imaging due to variations in source time function and earth structure. *Bulletin of the Seismological Society of America,* 104(2), 855-874 (2014).

8. Meng L., Ampuero J. P., Luo Y., Wu W., Ni S. Mitigating artifacts in back-projection source imaging with implications for frequency-dependent properties of the Tohoku-Oki earthquake. *Earth, planets and space*. Dec;64(12):1101-9 (2012).

9. Li, B., Wu, B., Bao, H., Oglesby, D. D., Ghosh, A., Gabriel, A. A., ... & Chu, R. Rupture Heterogeneity and Directivity Effects in Back-Projection Analysis. *Journal of Geophysical Research: Solid Earth,* 127(3), e2021JB022663 (2022). Minson, S. E., Simons, M., & Beck, J. L Bayesian inversion for finite fault earthquake source models I—Theory and algorithm. *Geophysical Journal International,* 194(3), 1701-1726 (2013)..

10. Spudich, P., & Cranswick, E. Direct observation of rupture propagation during the 1979 Imperial Valley earthquake using a short baseline accelerometer array. *Bulletin of the Seismological Society of America*, 74(6), 2083-2114 (1984).

11. Di Toro, G., Han, R., Hirose, T., De Paola, N., Nielsen, S., Mizoguchi, K., Ferri, F., Cocco, M. and Shimamoto, T., Fault lubrication during earthquakes. *Nature*, 471(7339), pp.494-498 (2011).

12. Fukuyama, E., Mikumo, T., and Olsen. K. B. Estimation of the critical slip-weakening distance: Theoretical background. *Bulletin of the Seismological Society of America* 93, no. 4: 1835-1840 (2003).

13. Fukuyama, E., and Mikumo. T. Slip-weakening distance estimated at near-fault stations, *Geophys. Res. Lett.* 34, no. 9, 2–6 (2007).

14. Chen, X., & Yang, H. Effects of seismogenic width and low-velocity zones on estimating slip-weakening distance from near-fault ground deformation. *Geophysical Journal International,* 223(3), 1497-1510 (2020).

15. Dunham, E. M., & Archuleta, R. J. Evidence for a supershear transient during the 2002 Denali fault earthquake. *Bulletin of the Seismological Society of America,* 94(6B), S256-S268 (2004).

16. Xu, S., Fukuyama, E., Yamashita, F., Kawakata, H., Mizoguchi, K., & Takizawa, S. Fault strength and rupture process controlled by fault surface topography. *Nature Geoscience,* 1-7 (2023).

17. Rubino, V., Rosakis, A. J., & Lapusta, N. Spatiotemporal properties of sub-Rayleigh and supershear ruptures inferred from full-field dynamic imaging of laboratory experiments. *Journal of Geophysical Research: Solid Earth*, 125(2), e2019JB018922 (2020)..

18. Kaneko, Y., Fukuyama, E., & Hamling, I. J. Slip-weakening distance and energy budget inferred from near-fault ground deformation during the 2016 Mw7. 8 Kaikōura earthquake. *Geophysical Research Letters,* 44(10), 4765-4773 (2017).

19. Fukuyama, E., & Suzuki, W. Near-fault deformation and Dc ″during the 2016 Mw7. 1 Kumamoto earthquake. *Earth, Planets and Space,* 68(1), 1-6 (2016).

20. Chen, X., Yang, H., & Jin, M. Inferring critical slip-weakening distance from near-fault accelerogram of the 2014 Mw 6.2 Ludian earthquake. *Seismological Research Letters*, *92*(6), 3416-3427 (2021).

21. Melgar, D., Taymaz, T., Ganas, A., Crowell, B. W., Öcalan, T., Kahraman, M., ... & Altuntaş, C. Sub-and super-shear ruptures during the 2023 Mw 7.8 and Mw 7.6 earthquake doublet in SE Türkiye (2023).

22. Mello, M., Bhat, H. S., & Rosakis, A. J.. Spatiotemporal properties of Sub-Rayleigh and supershear rupture velocity fields: Theory and experiments. *Journal of the Mechanics and Physics of Solids,* 93, 153-181 (2016).

23. Kondo, H. and Özalp, S., Primary surface rupture and slip distribution associated with the Mw 7.8 earthquake in southern Turkey. Geological Survey of Japan web site (2023). https://www.gsj.jp/en/hazards/earthquake-hazards/turkey20230309.html

24. Rosakis, A., Abdelmeguid, M., & Elbanna, A. Evidence of Early Supershear Transition in the Mw 7.8 Kahramanmara\c {s} Earthquake From Near-Field Records. arXiv preprint arXiv:2302.07214 (2023).

25. Cruz-Atienza, V. M., Olsen, K. B., & Dalguer, L. A. Estimation of the breakdown slip from strong-motion seismograms: Insights from numerical experiments. *Bulletin of the Seismological Society of America*, *99*(6), 3454-3469 (2009).

26. Karabacak, V., Özkaymak, Ç., Sözbilir, H., Tatar, O., Aktuğ, B., Özdağ, Ö. C., ... & Arslan, G. The 2023 Pazarcık (Kahramanmaraş, Türkiye) Earthquake (Mw: 7.7): Implications for surface rupture dynamics along the East Anatolian Fault Zone. *Journal of the Geological Society*, jgs2023-020 (2023).

27. Guatteri, M., & Spudich, P. What can strong-motion data tell us about slip-weakening fault-friction laws?. *Bulletin of the Seismological Society of America,* 90(1), 98-116 (2000).

28. Weng, H., & Yang, H. Constraining frictional properties on fault by dynamic rupture simulations and near-field observations. *Journal of Geophysical Research: Solid Earth*, *123*(8), 6658-6670 (2018).

29. Yao, S., & Yang, H. Rupture dynamics of the 2012 Nicoya Mw 7.6 earthquake: Evidence for low strength on the megathrust. *Geophysical Research Letters*, *47*(13), e2020GL087508 (2020).

30. Aagaard, B. T., Knepley, M. G., & Williams, C. A. A domain decomposition approach to implementing fault slip in finite-element models of quasi-static and dynamic crustal deformation. *Journal of Geophysical Research: Solid Earth*, *118*(6), 3059-3079 (2013).

31. Burridge, R. Admissible speeds for plane-strain self-similar shear cracks with friction but lacking cohesion. *Geophys. J. Int*. 35 439–455 (1973).

32. Weng, H., Ampuero, JP. Continuum of earthquake rupture speeds enabled by oblique slip. *Nat. Geosci.* **13**, 817–821 (2020).

33. Boore, D. M. Effect of baseline corrections on displacements and response spectra for several recordings of the 1999 Chi-Chi, Taiwan, earthquake. *Bulletin of the Seismological Society of America*, *91*(5), 1199-1211 (2001).

34. Wang, R., Schurr, B., Milkereit, C., Shao, Z., & Jin, M. An improved automatic scheme for empirical baseline correction of digital strong-motion records. *Bulletin of the Seismological Society of America*, *101*(5), 2029-2044 (2011).

Data and Materials Availability

The data used in this study are strong motion data downloaded from AFAD-TADAS website (https://tadas.afad.gov.tr).

Supplementary Materials

Methods and Materials

Figure S1-S9

Table S1

References (29-32)

Figures

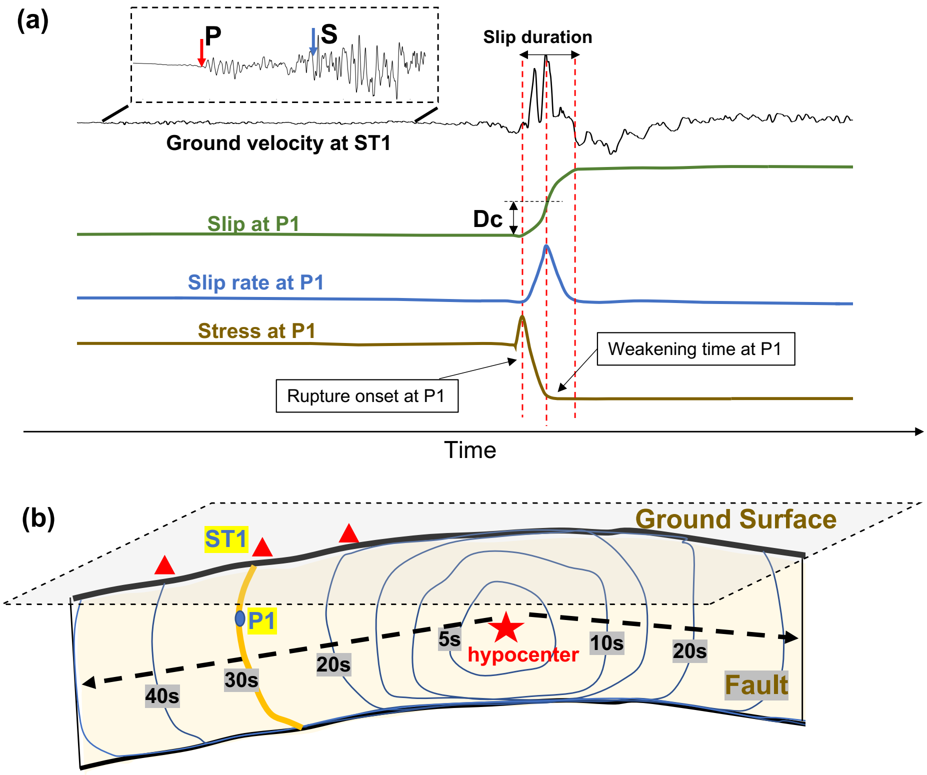

Figure 1: Schematic plot for rupture propagation and near-fault velocity waveforms. (a) The stress (brown), slip rate (blue), and slip (green) evolution on the fault at point P1 and the waveforms observed on the near-fault station ST1. The red dashed lines mark the time of the rupture (slip) onset, the peak slip rate (the weakening time), and the end of the slip at P1. The zoom-in window shows the P and S waves radiated from the hypocenter received on the station ST1. (b) A schematic plot showing the rupture propagation process on a fault and near-fault stations on the surface ground.

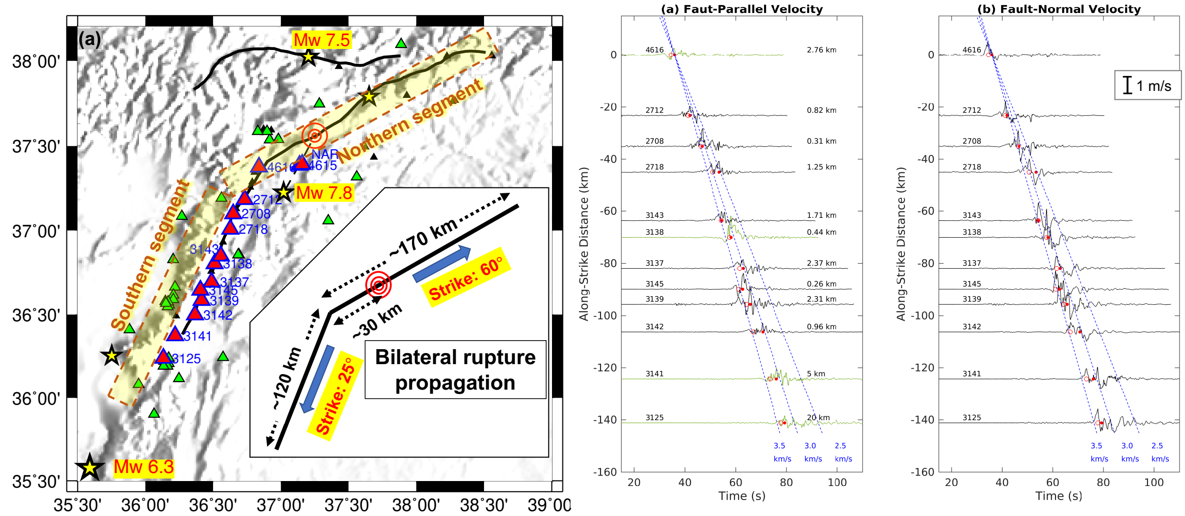

Figure 2: (a) A map of the Turkey earthquake sequence region. The yellow stars indicate the hypocenters of the Mw 7.8, the Mw 7.5, and the Mw 6.3 earthquakes (locations from USGS). The black thick line is the fault trace determined by InSAR, provided by Prof. XU Wenbin from Central South University. The red triangles with blue outline except the southernmost two (3141 and 3125) mark the strong motion stations located within 3 km to the fault trace. The green triangles with black outline are strong motion stations within 50 km to the fault trace. The small black triangles mark stations with problematic data. The inset panel shows the simplified 2-segment fault rupture model with strike and extent. Panels (b) and (c) show the velocity waveforms recorded on the near-fault strong motion stations in Fault-Parallel and Fault-Normal components, respectively, aligned by the mainshock origin time and sorted by the along-strike distance. The red dots and circles represent the times of peaks in the two components on each station, respectively. The dashed blue lines denote the synthetic times of peaks with different propagation speeds. The two stations 3138 and 4616 reside on the western side to the fault trace while others are on the eastern side. To keep the polarity consistent, the Fault-Parallel waveforms on the two stations are reversed (green).

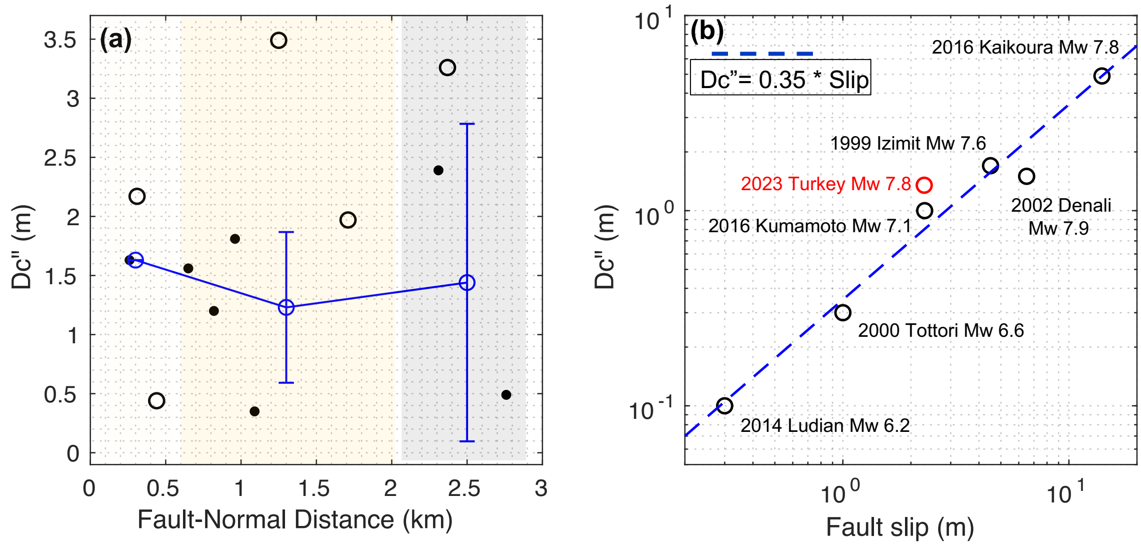

Figure 3: (a) The Dc'' versus the fault-normal distance on the 10 near-fault stations. The estimates on the 4 southernmost stations are marked as black circles as their waveforms feature high complexity which might lead to bias in the Dc'' estimation. Estimations on other stations are denoted by solid black dots. The blue line with error bars shows average Dc'' and standard deviations in three bins (with different gray levels as the background color). (b) The Dc'' versus fault slip that have been reported for previous earthquakes *(20)* (black circles) and the estimate for the Mw 7.8 Turkey earthquake in this study (red circle). The dashed blue line represents the empirical scaling law between the Dc'' and the local fault slip.

Supplementary Materials for

Rupture phase in near-fault records of the 2023 Turkey Mw 7.8 earthquake

Suli Yao (suliyao@cuhk.edu.hk) and Hongfeng Yang* (hyang@cuhk.edu.hk)

Earth and Environmental Sciences Programme, Chinese University of Hong Kong

Materials and Methods:

1, Determination of Vs and Vp from waveforms of the Mw 6.3 aftershock

The Mw 6.3 aftershock occurred on 20 Feb 2023, 14 days after the Mw 7.8 event. The location of this event is shown in figure 2a. The velocity waveforms in vertical component on the near-fault stations (red triangles in figure 2a) are illustrated in Figure S1. As expected, the amplitude of the waveforms decays from the south to the north with the epicentral distance. We pick the P and S arrivals on each station. Since the ray paths from this event to the stations are nearly parallel to the southern segment fault trace of the Mw 7.8 mainshock, the arrival time profile can be directly used to approximate the local P and S wave velocities. Then we infer the Vp and Vs to be 6.2 and 3.5 km/s, respectively, by fitting the arrivals (Fig. S1b).

2, Spectrograms of near-fault data of the Mw 7.8 earthquake

To verify whether those velocity pulses are surface waves, we calculate the spectrograms for the velocity waveforms on all near-fault stations. Surface waves always feature strong dispersion that the waves with different frequencies travel at different speeds. However, no dispersion has been identified in the spectrograms among all stations, which rules out the hypothesis of surface-wave pulses. As examples, here we show the results on two stations 3138 (Fig. S2) and 2718 (Fig. S3) in two horizontal components, respectively.

3, Dynamic rupture simulation

To verify whether the picked rupture phases can robustly represent the propagation of the rupture front on faults, we conduct 3-D dynamic rupture simulations for the Mw 7.8 Turkey earthquake. The model extends 300 km along strike (45° to the north, the average strike of northern and southern segments), 120 km in strike-normal direction, and 30 km in depth. We adopt the fault trace determined by InSAR to prescribe the fault (the black thick line in figure 2a). Since current reports for this event are all in agreement with a high-angle strike-slip fault, we assume the fault to be vertical (dip angle 90). The size of grids on the fault is 200 m and increases gradually to 3 km on the boundaries. We assume the effective normal stress to be 50 MPa on the fault. The shear stress is prescribed to be uniform inside the seismogenic depth (1-10 km) as 32 MPa. The shear stress outside the seismogenic zone is 20 MPa.

We adopt a slip-weakening friction law as the constitutive law on the fault. In this friction law, the frictional strength decreases linearly with fault slip and drops from yield stress (τ_s) to dynamic stress (τ_d) level when the slip reaches the critical weakening distance (Dc). The major parameters include the static friction coefficient, the dynamic friction coefficient, and the critical weakening distance. We choose typical values of 0.8 and 0.4 for static and dynamic friction coefficients. The stress ratio inside the seismogenic zone (S=$\frac{\tau_s-\tau_0}{\tau_0-\tau_d}$; $\tau_s = 40MPa, \tau_0 = 32\ MPa, \tau_d = 20MPa$) is 0.67, close to the value estimated by dynamic inversions for large earthquakes *(28,29)*. The Dc is prescribed to be 0.8 m, close to the range determined by near-fault records, as discussed in the main text.

We nucleate the rupture at the junction point between the major fault and the branch where the earthquake started. The nucleation depth is set to be 9 km, close to the down-dip bound of the seismogenic zone. We increase the initial shear stress to be 0.1 MPa higher than the yield stress inside a circular nucleation zone with a radius of 2 km. The rupture outside the nucleation zone is spontaneous under the control of the stress and friction evolution. We use a finite-element package, PyLith *(30)*, to run the simulation. The final slip, moment rate function, and surface rupture in the dynamic model are shown in Figure S4.

4, Rupture phase speed estimation

We pick a group of hypothesized stations at 1 km from the fault trace and inspect the synthetic ground velocity waveforms (Fig. S5). Velocities pulses are observed on those hypothesized stations. The peak ground velocities always occur close to the rupture onset with time differences within 2s, suggesting that the rupture phase can be used to track the rupture propagation. Based on the time of the peak velocities, we measure the average propagation speed of the rupture phase in the two components. The average rupture phase speed is estimated to be ~3.10 km/s and ~3.05 km/s along the southern and the northern segments, respectively, slightly lower than the rupture speed on the fault (~3.27 km/s and ~3.19 km/s on the southern and northern segments, respectively).

We pick the rupture phase with different distances to the fault trace to estimate the rupture phase speed (Fig. S6). We measure the speeds in two horizontal components and on both sides of the faults. Then we calculate the mean prediction and the standard deviations. The estimation generally decreases with the fault-normal distance and the standard deviation increases. Such instability in rupture phase speed when the distance is higher than 3 km is due to the loss of coherence in rupture phase along strike. As shown in figure S7, the synthetic waveforms at 10 km from the fault trace exhibit fluctuations in peak times.

To test the sensitivity of the rupture phase speed to the rupture speed on the fault and to quantify the uncertainty, we conduct models with different shear stress values and seismogenic depths to obtain models with different rupture speeds, including supershear cases (Table S1). Overall, the rupture phase speed increases with the rupture speed for both subshear and supershear ruptures (Fig. S8). The underestimation ranges from 2% to 7% among models. Since our models are nearly pure strike-slip, the rupture speed is either subshear or faster than the Eshelby speed ($\sqrt{2}$Vs), consistent with the prediction from the 2-D theory of fracture mechanics *(31)*. To further examine cases with continuous average rupture speeds, oblique slip *(32)* or heterogeneous initial condition should be considered.

5, The Dc'' estimation

To estimate the Dc'' from the strong motion data, we first integrate the acceleration to velocity and then to displacement in the F-P component. Then we pick the F-P displacement at the peak velocity. The double of this value is the Dc'' determined. When doing the integral from velocity to displacement, we find baseline shifts *(33)*. We correct for the baseline shifts following the method introduced in Wang et al. (2011) *(34)*. We find the baseline shifts on stations 2708, 2718, 3138 are very severe and the correction may significantly influence the Dc'' estimation. While the shifts are minor before the velocity peaks on other stations so that the estimation for Dc'' is relatively stable on the correction process (Fig. S9 and S10).

Figures S1-S9 and Table S1

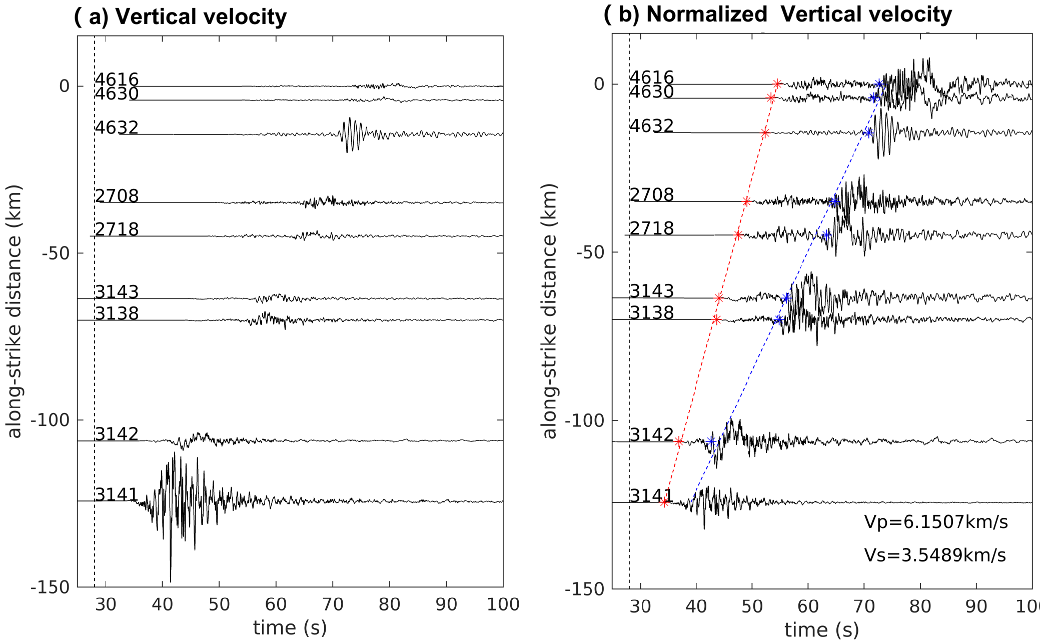

Figure S1: Vertical-component velocity waveforms along the southern segment caused by the Mw 6.3 earthquake in figure 2a. (a) the profile of waveform data with a uniform normalization, (b) the waveform data normalized individually. The red and blue asterisks mark the picked P and S arrival times. The dashed lines represent the best-fit speeds, written in the bottom right corner of the panel (b).

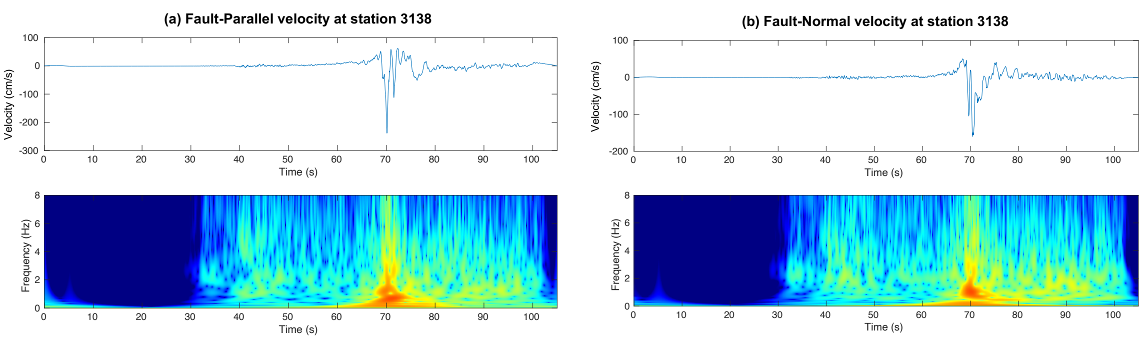

Figure S2: The velocity waveforms and the spectrograms at station 3138 in F-P (a) and F-N (b) components, respectively.

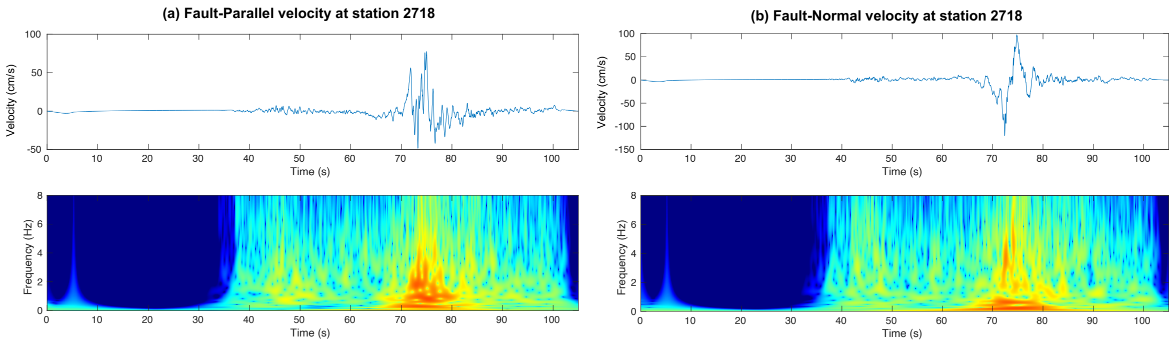

Figure S3: Same plot with figure S2 but the data are from the station 2718.

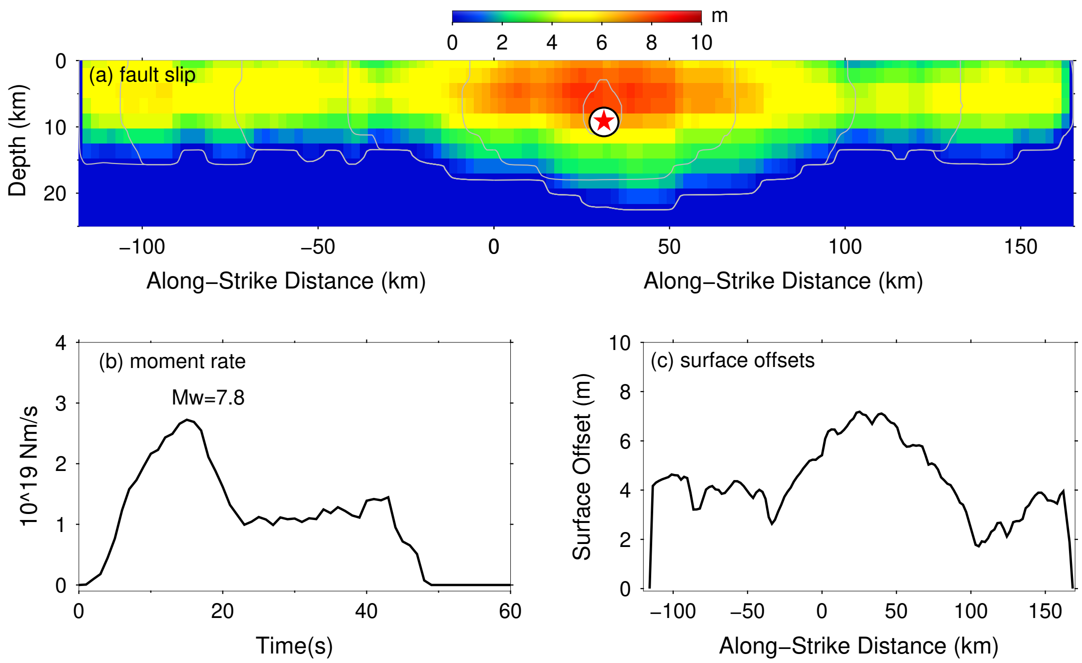

Figure S4: The dynamic rupture model for the 2023 Mw 7.8 Turkey earthquake. (a) Final slip distribution on the fault in a projected planar view. The red star marks the location of the nucleation zone. The gray contours are rupture fronts in every 10 seconds. (b) Moment rate function of the rupture model. (c) Surface offsets as a function of the along-strike distance.

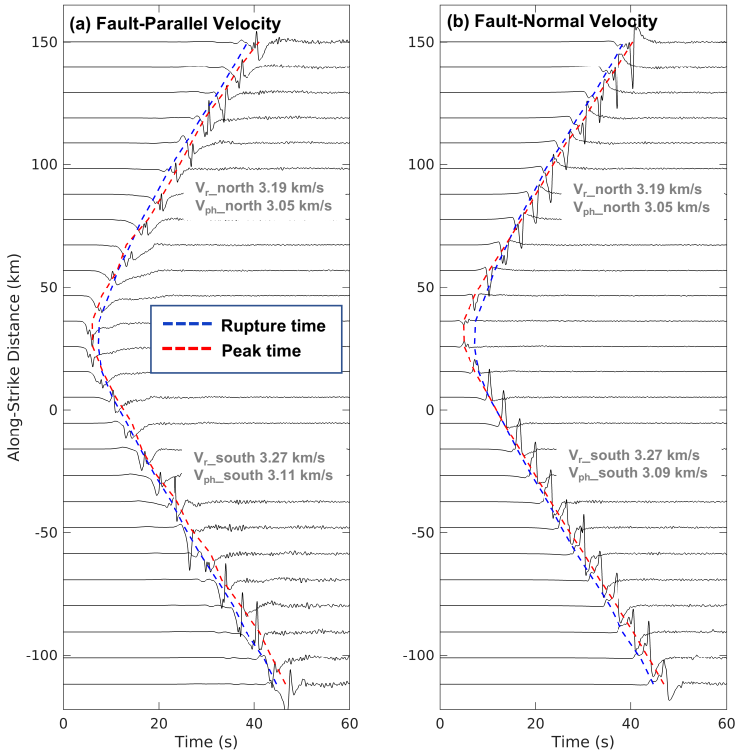

Figure S5: Synthetic ground velocity waveforms at 1km from the fault trace in F-P (a) and F-N (b) components. The blue dashed lines represent the average rupture onset time along strike. The red dashed lines mark the time of peak ground velocities. Vr_south (Vr_north): the average rupture speed on the fault along the southern (northern) segment. V_{ph}_south (V_{ph}_north): the average rupture phase speed along the southern (northern) segment.

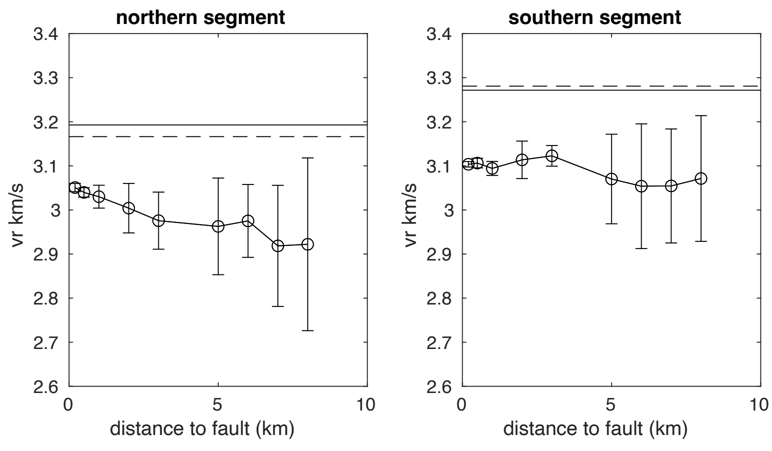

Figure S6: Rupture phase speed estimation versus distance to the fault. The error bar represents the standard deviation of rupture phase speed among estimations from two horizontal components and from both sides to the fault. The solid and dashed black horizontal lines represent the average rupture speed on the fault based on the rupture onset time (slip onset time) and the peak slip rate time on the fault.

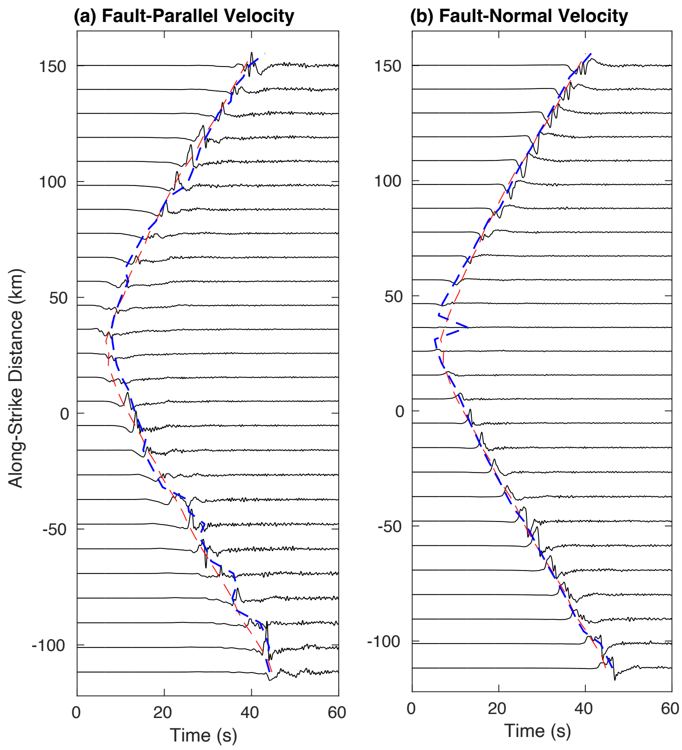

Figure S7: Same plot with figure S5 but at 10 km from the fault trace.

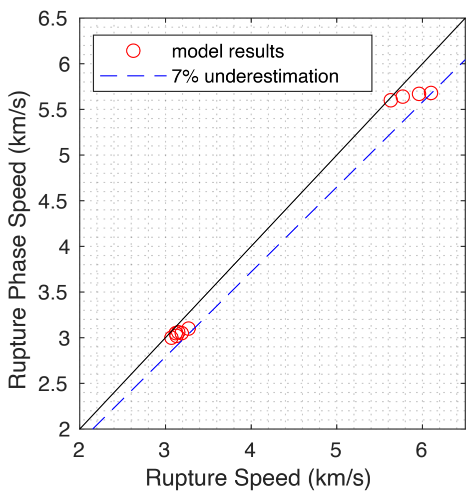

Figure S8: The rupture phase speed versus rupture speed on the fault in different models (Table S1). The black line is the reference line assuming that the two speeds are equal. The blue dashed line is the prediction of rupture phase speed with 7% underestimation for the rupture speed on the fault.

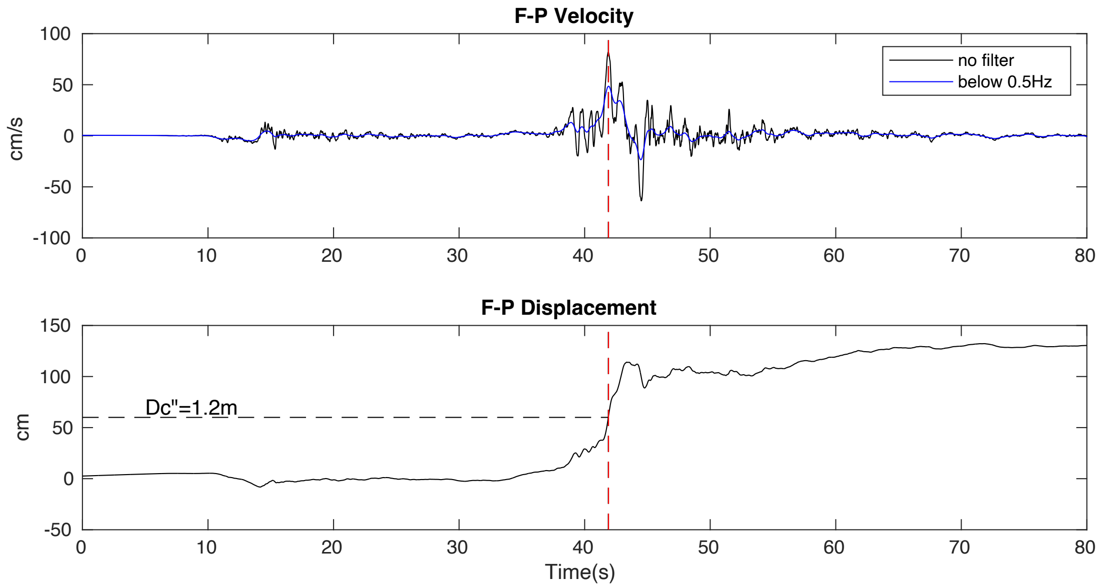

Figure S9: The velocity and displacement waveforms on the fault-parallel component of station 2712. The peak velocity is marked by red dashed lines. The Dc" values at this station is written in the displacement panel.

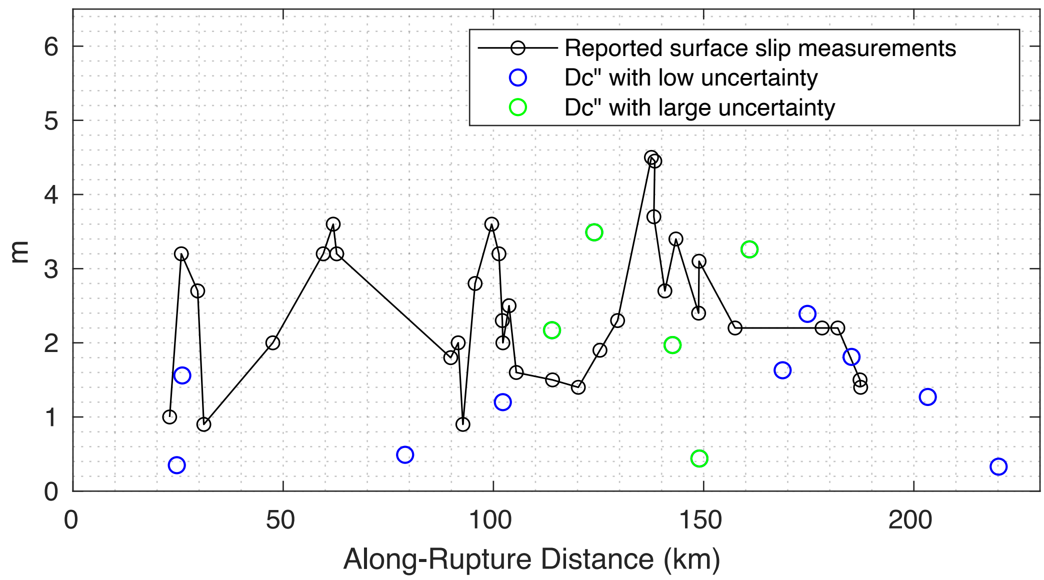

Figure S10: The determined Dc" (green and blue circles) and the reported surface slip (black circles) (Karabacak et al., 2023) along the rupture.

Model No.	Mw	Shear stress (MPa)	Seismogenic depth (km)	Rupture speed (North/South) (km/s)	Rupture phase speed (North/South) (km/s)	Underestimation (%)
1 subshear	7.8	32	10	3.27/3.19	3.10/3.05	4-5
2 subshear	7.7	30	10	3.13/3.07	3.02/3.00	2-4
3 subshear	7.9	30	15	3.15/3.12	3.06/3.05	2-3

4 supershear	8.1	32	15	5.96/6.10	5.67/5.68	3-7
5 supershear	8.0	32	12	5.77/5.63	5.64/5.60	0-3

Table S1 Results of dynamic rupture models with different initial conditions.